A Parallelizable Space-Time Approach in the Uzawa Solver with Multigrid for Poroelasticity

Vanessa Terezinha Ales[1]* , Márcio A.V. Pinto[1] , Sebastião R. Franco[2] , Simone F.T. Gonçalves[1]

[1] Department of Mechanical Engineering, Federal University of Paraná, Curitiba 81531-980, Brazil
[2] Department of Mathematics, State University of the Central West, Irati 84505-677, Brazil

Corresponding Author Email: vanessa.ales@ufpr.br

ABSTRACT

Poroelasticity studies fluid-solid interactions in deformable porous media, crucial for accurate models in engineering, medicine, and geology. It is represented by partial differential equations involving displacement and pressure, creating a saddle point problem that can cause numerical instabilities and hinder solutions. Traditional approaches rely on classical solvers and time sweeps. This article introduces a new approach combining advanced numerical methods with a space-time sweeping technique to address these challenges. Our study focuses on the 2D poroelasticity problem using the Finite Volume Method for spatial discretization and the implicit Euler method for time discretization. Unlike conventional methods, our approach uses a novel Uzawa solver with a distinct space-time sweep that decouples equations, allowing displacement calculations before pressure updates. Multigrid is integrated to improve convergence, especially for elliptic problems in the post-decoupling analysis. Our results highlight the effectiveness of the space-time sweep, with an average convergence factor below 0.31 across cases. These findings underline the potential of the proposed approach in solving complex real-world poroelasticity problems with enhanced computational efficiency. Computational time is greatly reduced compared to the Singlegrid method, achieving a speed-up of about 4800 on the 1024×1024 mesh. The space-time sweep is highly parallelizable, offering substantial advantages in processing time and convergence rates.

1. INTRODUCTION

Poroelasticity refers to the dynamic interrelation between fluid flow and solid deformation within porous media, characterized by solid structures containing fluid-filled pores. External loads exerted on the porous medium influence the entire system. Pressure variations within the fluid-filled pores subsequently influence fluid movement, while the solid material undergoes elastic deformation in response [1].

Karl von Terzaghi's (1883-1963) work on the one-dimensional theory of soil consolidation, rooted in empirical observations, and Maurice A. Biot's (1905-1985) approach, which incorporates the compressibility of the solid component within porous media, jointly established the framework for understanding the coupling between porous elastic solid deformation and the linear viscous fluid flow. Since then, it has been established that the principles of continuous poroelasticity and Darcy's law are derived from the microscopic Navier equations, which dictate the deformation of the elastic solid constituting the porous medium's solid component, and the Navier-Stokes equations, which govern flow at the pore scale [2].

The study of behavior in poroelasticity is fundamental for developing accurate models that describe porous materials across various contexts. Poroelasticity facilitates modeling applications such as subsurface exploration for oil [3, 4], groundwater flow using brine in porous media [5, 6], assessing displacements of geotechnical structures [7, 8], examining mechanical properties of bones and biological tissues [9-11], analyzing noise generated by pile driving in the wind power industry through seabed modeling [12], agricultural engineering [13] and numerous other applications.

The mathematical model of the poroelasticity problem encompasses two key relationships: the displacement and pressure of the fluid within the porous medium, and the structural displacement of the porous matrix, as elucidated by Biot's theory. This results in a system of equations comprising the momentum balance equation for the porous system and the mass conservation equation for the fluid within the pores.

One approach to solving the resultant system of differential equations is through numerical methods, necessitating the discretization of the differential equations. This discretization can be achieved using various techniques, including the finite difference method [14], and finite volume method [15], among others.

Saddle point problems frequently arise in the numerical analysis of solutions to partial differential equations (PDEs) with constraints, such as diffusion-advection problems, Stokes

problems, and Darcy problems. Effectively addressing saddle point problems necessitates the utilization of smoothers capable of efficiently managing the coupling between displacement and pressure [16].

Several studies have been conducted in the domain of poroelasticity problem resolution. Oosterlee and Gaspar [17] introduced the Vanka smoother, which addresses variables in a mutually dependent manner concerning both the Stokes equations and the incompressible poroelasticity problem, focusing on the 2D spatial context. Their findings indicated superior performance, particularly on collocated meshes.

Borregales et al. [18] proposed a methodology aimed at resolving the 2D and 3D poroelasticity problem, leveraging an updated version of the Fixed-Stress method. This approach integrates the temporal variable as an additional dimension to effectively parallelize the Biot problem. Through a series of numerical experiments and convergence analyses, they provided empirical evidence of the method's robustness.

The Parallel Full Approximation Scheme in Space and Time (PFASST) methodology operates by interleaving Spectral Deferred Corrections (SDC) iterations with varied resolutions, similar to the Parareal algorithm. It incorporates a Full Approximation Scheme (FAS) correction to enhance the accuracy of coarser SDC iterations. Parallelization along the time direction facilitates the computation of solutions at subsequent time steps based on solutions obtained at preceding time points, employing spectral corrections [19].

Franco and Pinto [20] employed colored ordering in conjunction with the Vanka smoother within the Finite Difference Method framework to address the poroelasticity problem. Their approach also integrated the Multigrid method and Waveform Relaxation temporal sweep technique.

Adler et al. [21] introduced a finite element discretization approach to tackle the poroelasticity problem. They developed block preconditioners coupled with Multigrid and Fixed-Stress techniques, demonstrating a robust methodology capable of accommodating fluctuations in physical parameters, mesh sizes, and time steps inherent to the poroelasticity problem.

The Uzawa solver stands as an efficient iterative technique for addressing saddle point systems. Due to its simplicity and low memory requirements, it has garnered extensive utilization [22]. Subsequently, recent investigations into the classical iteration of this method or its integration with other methodologies, aimed at enhancing convergence, are outlined.

Miao and Zhang [22] introduced the Uzawa Single-Step Iteration (Uzawa-SSI) method as a solution for both non-Hermitian nonsingular and singular saddle point problems. Their study involved a comparative analysis with other Uzawa variants, highlighting the simplicity of convergence conditions in Uzawa-HSS (Uzawa Hermitian and Skew-Hermitian Splitting). They provided numerical evidence showcasing the efficiency of the Uzawa-SSI method. However, it is worth noting that this method entails the evaluation of a parameter λ, which can pose challenges in practice.

Axelsson and Karátson [23] proposed a Krylov-Uzawa method tailored for the Stokes problem, aimed at accelerating convergence. Their analysis established that the Krylov-Uzawa iteration may demonstrate superlinear convergence.

Keram and Huang [24] devised a Uzawa-type algorithm leveraging the mixed finite element method for resolving the steady-state natural convection model. Comparing it with the conventional Uzawa algorithm, they noted a reduction in CPU time with the proposed approach.

Wu and Gao [25] introduced a diagonally preconditioned Uzawa Splitting method tailored for saddle point problems, offering a sufficient condition to guarantee convergence. Their findings illustrated that the proposed method outperforms certain existing methodologies in the literature. Furthermore, they observed that the preconditioner can enhance the efficiency of associated Krylov subspace methods.

Uzawa methods coupled with the Multigrid technique offer the benefit of accelerated convergence. This notion is supported by several references:

Luo et al. [26] implemented the Uzawa smoother in solving the 2D poroelasticity equations utilizing finite volume discretization, in conjunction with the Multigrid method. Their proposed smoother combines Symmetric Gauss-Seidel iterations for displacements with Richardson iterations for the Schur complement within the pressure field. The relaxation parameters were determined through Local Fourier Analysis. Numerical simulations corroborated the efficacy and reliability of the proposed approach.

Badea [27] showcased the convergence of Uzawa and Arrow-Hurwicz algorithms integrated with Multigrid for resolving general saddle point problems, characterized by constrained optimizations.

In a related study, Spies et al. [28] conducted a comparative analysis of three relaxation scheme options – Braess-Sarazin, Vanka, and Schur-Uzawa – utilizing a block triangular preconditioner and Multigrid method to address saddle point problems associated with the Stokes equations and the Oseen equation.

In contrast to previous works, this article proposes a solution to the poroelasticity problem through a novel parallelizable spatio-temporal scanning approach, combining the Uzawa method with Multigrid techniques.

The structure of the paper unfolds as follows: Section 2 delineates the mathematical and numerical models underpinning the problem; Section 3 delineates the Multigrid method; Section 4 introduces the novel time sweep method; Section 5 elucidates the numerical outcomes of the simulations; and finally, Section 6 encapsulates the conclusions drawn from the study.

2. MATHEMATICAL AND NUMERICAL MODELS

2.1 Poroelasticity equations

The classical formulation of the poroelasticity problem assumes a saturated, homogeneous, and isotropic porous medium, along with an incompressible fluid [29]. The two-dimensional problem is described by the system of differential equations Eqs. (1)-(3):

$$-(\lambda + 2\mu)\frac{\partial^2 u}{\partial x^2} - \mu\frac{\partial^2 u}{\partial y^2} - (\lambda + \mu)\frac{\partial^2 v}{\partial xy} + \frac{\partial p}{\partial x} = \mathcal{U} \qquad (1)$$

$$-(\lambda + \mu)\frac{\partial^2 u}{\partial xy} - \mu\frac{\partial^2 v}{\partial x^2} - (\lambda + 2\mu)\frac{\partial^2 v}{\partial y^2} + \frac{\partial p}{\partial y} = \mathcal{V} \qquad (2)$$

$$\frac{\partial}{\partial t}\left(\frac{\partial u}{\partial x} + \frac{\partial v}{\partial y}\right) - K\left(\frac{\partial^2 p}{\partial x^2} + \frac{\partial^2 p}{\partial y^2}\right) = \mathcal{P} \qquad (3)$$

The terms $\lambda = \frac{\nu E}{(1+\nu)(1-2\nu)}$ and $\mu = \frac{E}{2(1+\nu)}$ denote the Lamé constants, which are related to Young's modulus E and

Poisson's ratio ν (shear of homogeneous and isotropic materials). Here, K represents the hydraulic conductivity, expressing the ease of fluid movement within the solid matrix of the porous medium.

The terms $\mathcal{U}$ and $\mathcal{V}$ denote the density of the force applied to the body, while $\mathcal{P}$ represents the force of fluid injection or extraction within the porous medium.

The variables of interest include the displacement, represented by $u(x,y,t)$ and $v(x,y,t)$ and the pressure, denoted by $p(x,y,t)$, which depend on spatial position and time, as well as the time interval $(0, t_f]$, where, t_f signifies the final time, and the two-dimensional spatial domain Ω. This problem incorporates boundary conditions featuring fixed displacement and free drainage, commonly referred to as Dirichlet conditions, which can be applied in a reservoir simulation, i.e., $u_b = v_b = p_b = 0$ [26, 30, 31].

For comparison purposes, analytical solutions given by the following functions have been proposed:

$$u = v = p = \sin(\pi x)\sin(\pi y)e^{-t} \qquad (4)$$

Thus, the source terms fulfilling the problem were derived, represented by the functions:

$$\mathcal{U} = \pi e^{-t}(\lambda + 3\mu)\pi \sin(\pi x)\sin(\pi y) + \\ -\pi e^{-t}(\cos(\pi x)((\lambda+\mu)\pi\cos(\pi y) + \sin(\pi y))) \qquad (5)$$

$$\mathcal{V} = \pi e^{-t}(\lambda + 3\mu)\pi\sin(\pi x)\sin(\pi y) + \\ -\pi e^{-t}\left(\cos(\pi y)((\lambda+\mu)\pi\cos(\pi x) + \sin(\pi x))\right) \qquad (6)$$

$$\mathcal{P} = \pi e^{-t}2K\pi\sin(\pi x)\sin(\pi y) \\ -\pi e^{-t}\sin(\pi(x+y)) \qquad (7)$$

Gaspar et al. [32] introduced a reformulated version of the problem, incorporating an additional smoothing term in the pressure equation (Eq. (3)). This term, aimed at enhancing the stability of the system for numerical solutions, is expressed as follows:

$$-\frac{h^2}{4E}\frac{\partial}{\partial t}\left(\frac{\partial^2 p}{\partial x^2} + \frac{\partial^2 p}{\partial y^2}\right) \qquad (8)$$

2.2 Discretization of the mathematical model

The spatial domain Ω is discretized utilizing the Finite Volume Method, employing a uniform mesh that subdivides it into control volumes with uniform spacings h_x and h_y, respectively in the x and y directions, composing a mesh such that each point of the mesh is centered on a volume. A typical central control volume, with its central point being P, and the adjacent volumes are represented in Figure 1.

The points of the surrounding volumes are indicated by W, E, S, and N, representing the west, east, south, and north neighboring volumes, respectively. The faces between these volumes and the central volume P are indicated by the corresponding lowercase letters. The adopted mesh adheres to the characteristics depicted in Figure 1, featuring a uniform orthogonal mesh with a collocated arrangement. The nodal points are situated at the center of each control volume, implying that the pressure p and the displacements u and v are located at the center of the control volume.

After discretizing the domain, the governing equations are integrated over each control volume utilizing the Gauss Divergence Theorem [33]. This entails evaluating the integrals of spatial derivatives through the corresponding fluxes on the faces of the volumes. These fluxes are approximated by discrete differences involving neighboring control volumes. The derivatives are approximated using second-order Central Difference Schemes (CDS), while the integral of the source term over the control volume is approximated using the midpoint rule [15].
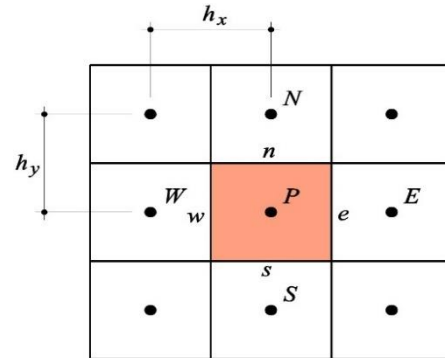

Figure 1. 2D mesh and representation of the central control volume

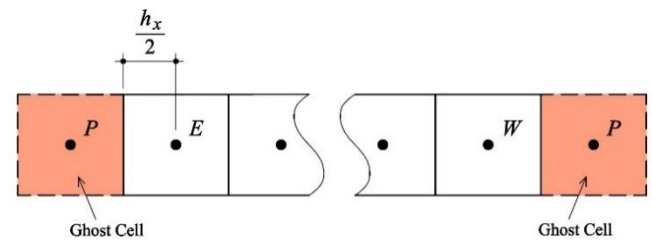For the boundary conditions, the ghost cells technique was employed, as depicted in Figure 2 [15].

Figure 2. Representation of the ghost cell

Considering a uniform mesh, the spatial domain $\Omega = [0,L] \times [0,L]$ is divided into N_x control volumes in the x-direction and N_y in the y-direction, resulting in $h_x = \frac{L}{N_x}$, $h_y = \frac{L}{N_y}$. In this work, $h = h_x = h_y$. The temporal approximation and the spatial/temporal connection are made using the Implicit Euler method. The time step τ is defined as $\tau = \frac{t_f - t_0}{N_t}$, where, t_f represents the final time, t_0 depicts the initial time, and N_t signifies the number of time steps.

Adding Eq. (8) to the left side of Eq. (3) and discretizing the new Eqs. (1)-(3), we have the system of equations formed by:

$$\frac{(2\lambda + 6\mu)}{h^2}u_P - \frac{(\lambda + 2\mu)}{h^2}(u_E + u_W) - \frac{\mu}{h^2}u_N \\ -\frac{\mu}{h^2}u_S + \frac{\lambda+\mu}{4h^2}(v_{NE} - v_{NW} - v_{SE} + v_{SW}) \\ +\frac{1}{2h}(p_E - p_W) = \mathcal{U} \qquad (9)$$

$$\frac{(2\lambda + 6\mu)}{h^2}v_P - \frac{\lambda + 2\mu}{h^2}(v_N + v_S) - \frac{\mu}{h^2}v_E \\ -\frac{\mu}{h^2}v_W + \frac{\lambda+\mu}{4h^2}(u_{NE} - u_{NW} - u_{SE} + u_{SW}) \\ +\frac{1}{2h}(p_N - p_S) = \mathcal{V} \qquad (10)$$

$$\frac{4\tau K(\lambda + 2\mu) + h^2}{\tau h^2(\lambda + 2\mu)}p_P - \frac{(4\tau K(\lambda + 2\mu) + h^2)}{\tau h^2(\lambda + 2\mu)}p_E$$
$$- \frac{(4\tau K(\lambda + 2\mu) + h^2)}{\tau h^2(\lambda + 2\mu)}(p_W + p_N + p_S)$$
$$+ \frac{1}{2h\tau}(u_E - u_W + v_N - v_S) = \mathcal{P} \qquad (11)$$
$$- \frac{1}{2h\tau}(u_E^0 - u_W^0 + v_N^0 - v_S^0)$$
$$+ \frac{1}{4\tau(\lambda + 2\mu)}(p_E^0 + p_W^0 - 4p_P^0 + p_N^0 + p_S^0)$$

It is worth noting that in Eq. (11), the values of the displacement and pressure variables at the previous time step are required for the calculation of the current variable, represented by u^0, v^0, and p^0.

Impermeable conditions are applied to the outer boundary of the porous medium, so that, for simplicity, both the boundary and the initial conditions lead to the proposed solution [20].

2.3 Physical parameters

The hydraulic conductivity K of the soil, closely associated with hydraulic permeability κ, represents a constant indicating the ease with which water permeates through it, holding significant importance for soil and water management [1]. Various values of K are provided in Table 1.

Table 1. Realistic values of hydraulic permeability (κ) and hydraulic conductivity (K)

Type of Rock	Hydraulic Permeability κ [m^2]	Hydraulic Conductivity K [m/s]
Sand to sandstone	10^{-12}	10^{-5}
Sandstone to limestone	10^{-15}	10^{-8}
Granite to shale	10^{-18}	10^{-11}

According to Ranjan and Rao [34], the value of Young's modulus of soil elasticity varies depending on factors such as the historical stress value, density, and the presence of water. These values are typically derived from laboratory testing, pile loading tests, or empirical correlations based on experience. The following Table 2 correlates the soil type with the range of Young's modulus of elasticity [34].

Table 2. Realistic values of Young's modulus of elasticity

| Soil Type	Soil Density	Modulus of Elasticity E [MPa]
Silt	very soft	0.2-2
Clay	very soft to hard/sandy	2-500
Sand/gravel	silty/loose to dense	7-190

3. MULTIGRID AND SOLVERS

The Eqs. (9)-(11) give rise to large-scale sparse linear systems, for which direct methods are not recommended [14]. Classical iterative techniques for solving such linear systems, such as Gauss-Seidel methods, excel at eliminating only the oscillatory components of errors associated with dependent variables (high-frequency Fourier modes). However, they typically struggle to efficiently eliminate smooth error components (low-frequency Fourier modes). As a result, these methods are often referred to as smoothers, given their tendency to smooth out errors. Consequently, at the outset of the iterative process, a high convergence rate is observed, stemming from the rapid elimination of oscillatory components [35].

The Multigrid method's effectiveness lies in its ability to solve systems of equations, both linear and nonlinear, by employing multiple grid levels. This approach accelerates the convergence of the iterative method used for smoothing by going through the entire spectrum of Fourier error modes, thereby transforming smooth error modes into more oscillatory ones.

The Multigrid cycle combines iterations on fine and coarse grids, starting at the finest grid level (referred to as h), smoothing the system of equations, and then restricting to the immediately coarser grid (denoted as $2h$). This process iterates until reaching the coarsest grid level, followed by prolongation and return to the immediately finer grid. The method involves alternating restriction and interpolation operations between fine and coarse grids.

As outlined by Wesseling [36], the sequence in which the various grids are traversed determines the Multigrid cycle. The most prevalent cycles include the V, W, and F types. The W-cycle is adopted in this article for its robustness, as it is the preferred choice for problems involving poroelasticity [17, 37]. Figure 3 illustrates a W-cycle for four levels of grids, i.e., ngl=4, where ngl is the number of grid levels.
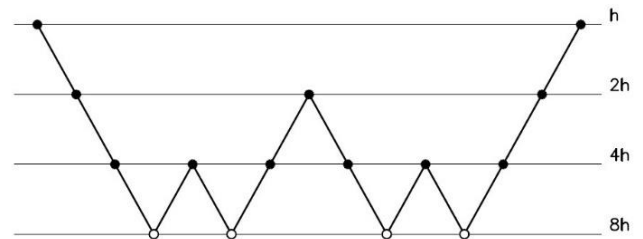
Figure 3. Representation of the W-cycle for 4 levels of grid

In the context of transferring information among different grids, the choice between residue and/or solution transfer depends on the nature of the problem. For linear problems, the correction scheme (CS) is deemed more suitable as it exclusively transfers the residue. Conversely, for nonlinear problems, the full approximation scheme (FAS) is preferred as it transfers both residue and solution [35, 36]. Given that the problem under consideration in this work is fundamentally linear, only the CS scheme is employed. Algorithm 1 outlines a W-cycle with CS.

In this algorithm, A represents the coefficient matrix, while f denotes the vector of independent terms obtained by discretizing the Eqs. (5)-(7).

Here, Λ represents a generic variable, and $\bar{\Lambda}$ is its approximation. I_h^H and I_H^h represent, respectively, the space restriction and prolongation operators (utilized at each time step), while v_1 and v_2 indicate the numbers of pre- and post-smoothing steps, respectively.

Within the Multigrid method, various smoothers can be employed, including classical solvers such as Gauss-Seidel with different formulations like Zebra, Red Black, and incomplete LU decomposition [32]. Zebra-type smoothers involve partitioning the domain into planes, sequentially solving each odd plane before addressing each even plane independently [19].

Algorithm 1. MG-W-cycle (l)
if $\quad l$ represents the coarsest grid level **then**
$\quad$ Solve system $A^{(l)} \Lambda^{(l)} = f^{(l)}$ in the coarsest grid $\Omega^{2^{(l-1)}h}$
else
$\quad$ Smooth ν_1 times $A^{(l)} \Lambda^{(l)} = f^{(l)}$ in grid $\Omega^{2^{(l-1)}h}$
$\quad$ Calculate and restrict the residual
$\quad f^{(l+1)} = I_{2^{(l-1)}h}^{2^l h} \left(f^{(l)} - A^{(l)} \overline{\Lambda}^{(l)} \right)$
$\quad$ **for** $\quad$ cycle $= 1:2$ **do**
$\quad\quad$ Solve in the next grid MG-W-cycle ($l+1$)
$\quad$ **end**
$\quad$ Interpolate and correct the approximation with
$\quad \overline{\Lambda}^{(l)} \leftarrow \overline{\Lambda}^{(l)} + I_{2^l h}^{2^{(l-1)}h} \overline{\Lambda}^{(l+1)}$
$\quad$ Smooth ν_2 times $A^{(l)} \Lambda^{(l)} = f^{(l)}$ in grid $\Omega^{2^{(l-1)}h}$
end

The Uzawa method is a smoother that involves decomposing the coefficient matrix obtained in the discretization (Eqs. (9-11)) into two matrices, as described in the system of equations Eq. (12) [38, 26]:

$$\begin{bmatrix} A & B^t \\ B & -C \end{bmatrix} = \begin{bmatrix} M_A & 0 \\ B & -\omega^{-1}I \end{bmatrix} - \begin{bmatrix} M_A - A & -B^t \\ 0 & C - \omega^{-1}I \end{bmatrix} \quad (12)$$

where, ω is a positive term called the relaxation parameter and M_A represents a preconditioner for the positive definite matrix A that makes the process less expensive for each iteration.

The matrix B represents the negative discrete divergence matrix, B^t stands for the discrete gradient matrix, and I denotes the identity matrix. C is a diagonal matrix primarily comprising negligible values due to its composition of hydraulic permeability, which tends to be very small. Additionally, it integrates the time discretization parameter τ as a multiplication factor, which can be arbitrarily small.

As a solver, Uzawa utilizes the Symmetric Gauss-Seidel method, which can be described as an incomplete LU decomposition [26].

The algorithm for the standard Uzawa method involves updating the variables $\boldsymbol{u} = (u, v)$ (displacement) and p (pressure) vectors based on their values at the previous iteration $\boldsymbol{u}^0$ and p^0 as described below:

$$\boldsymbol{u} = A^{-1}(\mathcal{U} - B^t \boldsymbol{u}^0) \quad (13)$$

$$p = p^0 + \omega(B\boldsymbol{u} - \mathcal{P}) \quad (14)$$

Therefore, the decoupled Uzawa method is equivalent to one iteration of the Richardson method, which can be employed to determine an optimal ω in terms of the maximum and minimum eigenvalues of the Schur complement matrix $S = BA^{-1}B^t$ [39, 40].

Luo et al. [26] conducted a systematic analysis of the relaxation parameter ω using Local Fourier Analysis, convergence, and acceleration techniques to enhance efficiency and accuracy in solving complex poroelastic problems.

The algorithm for the solution using the Uzawa smoother initially smooths the $\boldsymbol{u}$ vector for all control volumes, using p^0 and $\boldsymbol{u}^0$. The systems of this iterative process make use of the Symmetric Gauss-Seidel method as a solver. Subsequently, with this data, the pressure residual is determined and then p is updated.

Algorithm 2. Uzawa (l)
for $\quad It_{int} = 1 : it_{uv}$ **do**
$\quad$ Solve the system given by Eqs. (9)-(10) using MG-W-cycle (1)
else
Compute $res(p)$ (given by Eq. (11))
Update the variable $p \leftarrow p + \omega . res(p)$

Above is Algorithm 2 for solving the poroelasticity problem using the Uzawa method with Multigrid:

Unlike the classical Uzawa solver, here we propose Multigrid in the inner step (and in this case, limited to two cycles). In this algorithm, It_{int} represents the number of inner smoothings, it_{uv} denotes the number of smoothings of the displacement variables u and v that are performed within the W-cycle, $res(p)$ corresponds to the residue of the pressure, and ω depicts the relaxation parameter that is calculated on the finest grid in the Multigrid cycle, defined for $\tau = 1$ by [26]:

$$\omega = \frac{2h^2(\lambda + 2\mu)}{10K(\lambda + 2\mu)} \quad (15)$$

4. NOVEL TEMPORAL SWEEP METHOD

The time-stepping approach is a classical method for solving transient problems, yet it lacks the capability to parallelize the time variable. In the current era of advanced technologies and high-performance computing, there is a pressing need to devise algorithms capable of leveraging a large number of cores for data processing. This is crucial for enhancing efficiency in solving problems involving partial differential equations (PDEs) [41].

Another temporal sweep method known in the literature is Waveform Relaxation (WR) [42]. WR is an iterative method applied to time-dependent PDEs, where the spatial domain is decomposed into a set of points. For each point, a system of Ordinary Differential Equations (ODEs) is solved over all time intervals. This method enables the parallelization of algorithms for time-dependent PDEs, allowing each temporal ODE to be solved at all spatial nodes separately. The update of unknowns can then be performed at the end of a WR cycle [41].

Additionally, there is the Space-Time (ST) temporal sweep [43], which has a specific characteristic for the Multigrid method. It adopts a semi-coarsening strategy in space and time based on the anisotropy factor, which is the ratio between the time and space steps at each grid level. Space-time methods offer advantages when local refinement in the space and time domain is required. This method is characterized by using a point smoother, where at each iteration, all points in space and time have their information updated [44, 45].

Franco and Pinto [20] describe an adaptation of the Space-Time (ST) method. Its components are based on an adaptive smoothing strategy utilizing zebra-type relaxation in the xt and yt planes, and standard coarsening using Red-Black smoothing for the Multigrid method in the xy plane.

In this work, we propose a new space-time sweep, described in Algorithm 3, where I_h^H and I_H^h are, respectively, the space-time restriction and prolongation operators; h represents the spacing in the fine mesh, H represent the spacing in the coarse mesh; and ν_1 and ν_2, represent the numbers of pre- and post-smoothing, respectively.

Algorithm 3. New-STMG-W-cycle (l)
Input data
Compute coefficients and source terms
Compute u, v and p for all control volumes
Compute residuals of u, v, and p
while   not reaching the stopping criterion
if l is the coarsest grid level
Solve the system given by Eqs. (9)-(11) on grid $\Omega^{2^{(l-1)}h}$ using Uzawa (l)
else
Smooth ν_1 times the system given by Eqs. (9)-(11) on grid $\Omega^{2^{(l-1)}h}$ using Uzawa (l)
Calculate and restrict constrain the residue of u, v and p with operator $I_{2^{(l-1)h}}^{2^l h}$
for $It_{int} = 1 : 2$ **do**
Solve the system given by Eqs. (9)-(11) using New-STMG-W-cycle ($l + 1$)
end
Interpolate and correct the approximation with $I_{2^l h}^{2^{(l-1)}h}$
Smooth ν_2 times given by Eqs. (9)-(11) on the grid $\Omega^{2^{(l-1)}h}$
end
end

It is evident that such a sweep is highly parallelizable, as it facilitates parallelization in both time and space. Note that steps 7 and 9 of Algorithm 3 can be executed for all time steps in parallel, and step 2 of Algorithm 2 can be performed using a parallel solver in space.

The Multigrid method exhibited a high convergence rate, as demonstrated by the convergence factor, which is consistent with the results reported in the literature. In this article, in addition to applying Multigrid, we employ the Uzawa method and propose the decoupling of displacement and pressure variables, enabling parallel execution to obtain the solution.

The Multigrid method was applied in two stages: first, during the smoothing process using the Uzawa method to update the displacement and pressure variables; and second, in the smoothing of the variables associated with displacement, using stationary equations. The combination of the Multigrid method with the sweeping approach in the Uzawa solver provided significant benefits, including improved convergence speed and a reduction in the number of Multigrid cycles, in line with the literature.

5. NUMERICAL RESULTS

In this section, we present some numerical experiments aiming to demonstrate the robustness, efficiency, and good performance of the proposed Space-time Multigrid method outlined in the previous section. For this paper, we relied on Wang [1], which utilizes the values of the constants E (Young's modulus) and K (hydraulic conductivity) with realistic values, chosen as follows:

Case 1: $K = 1$ and $E = 1$ for verification purposes;

Case 2: $K = 10^{-9}$ and $E = 10^6$ representing a material equivalent to clay;

Case 3: $K = 10^{-6}$ and $E = 10^4$ representing a material equivalent to silt;

Case 4: $K = 10^{-3}$ and $E = 10^6$ representing a material equivalent to sand.

For comparison purposes, we used the same relaxation parameter ω, time step Δt and mesh size h parameters as in the study [26].

5.1 Computational details

For the proposed problem, we utilized the W-cycle Multigrid method, employing a full weighting restriction operator and a piecewise constant interpolation operator [15]. The choice of the W-cycle is consistent with reference [37], which asserts that the W-cycle is more robust than the V-cycle for poroelasticity problems. We set $\nu_1 = \nu_2 = \nu = 1$ for both pre- and post-smoothing. For relaxation in the plane, the Uzawa solver is applied with $it_{MC} = 2$ for the variables u and v, where it_{MC} denotes the number of Multigrid cycles. The parallelizable Symmetrical Gauss-Seidel Red-Black method is used. The number of grid levels (ngl) for Multigrid was limited to $ngl = 13$, i.e., $N_{xy} = N_x \times N_y = 2^{13} \times 2^{13} = 8192 \times 8192$ volumes in the spatial mesh, and in Singlegrid with $N_{xy} = N_x \times N_y = 2^{10} \times 2^{10} = 1024 \times 1024$ volumes in the spatial mesh. These limits were set due to memory and computational time usage, respectively. Additionally, the final time was defined as $t_f = 10$ s. The stopping criterion was based on the reduction of the dimensionless residual from the initial estimate, set to 10^{-8}, as follows:

$$res = \| res_u \|_\infty + \| res_v \|_\infty + \| res_p \|_\infty, \qquad (16)$$

where res_u, res_v and res_p represent, respectively, the residue obtained in the variables u, v, and p [20, 46].

The computational code was implemented using MATLAB R2023b - Academic. The tests were conducted on a computer equipped with a 13th Gen Intel (R) Core (TM) i5-13600K processor running at 3500 Mhz, featuring 14 cores and 20 logical processors, with 64 GB of RAM, and a 64-bit Microsoft Windows 11 Home operating system.

The verification of the code used in this article was carried out by comparing the solutions with those presented in Luo et al. [26] and Franco et al. [30].

The results were obtained using the implicit Euler method, which is unconditionally stable [14], and tested in conjunction with Multigrid.

5.2 Singlegrid and Multigrid comparison

In this work, to compare the performances of the Singlegrid and Multigrid methodologies, the average convergence factor, the order of complexity, and speed-up are employed.

5.2.1 Convergence factor

The convergence factor, which approximates the asymptotic convergence factor, is calculated by [35]:

$$\rho = \frac{\| res_{MC} \|_\infty}{\| res_{MC-1} \|_\infty} \qquad (17)$$

where, res_{MC} represents the value of the residual in the MC-th Multigrid cycle or iteration of the Singlegrid. Thus, the average convergence factor is given by:

$$\rho_m = {}^{MC}\sqrt{\frac{\|\,res_{MC}\,\|_\infty}{\|\,res_0\,\|_\infty}} \tag{18}$$

where, res_0 denotes the value of the residual in the initial estimate.

In Figure 4, the comparison of the average convergence factor ρ_m with mesh refinement for the Multigrid method (MG) and Singlegrid (SG) is presented, considering the constants K and E for the 4 cases studied. Here, ngl denotes the number of grid levels in the Multigrid method and represents 2^{ngl} control volumes in each spatial direction.
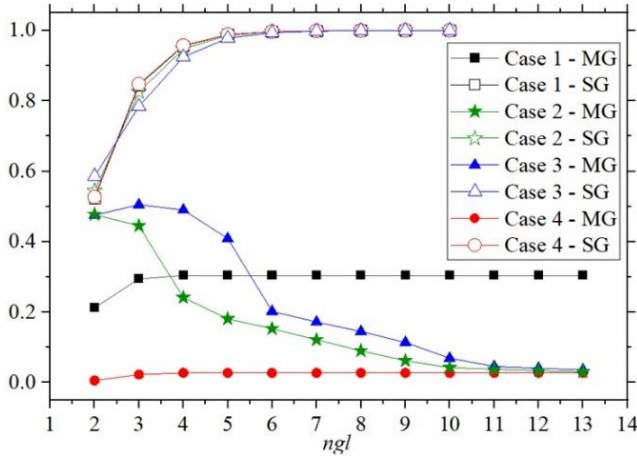
Figure 4. Comparison of ρ_m between Singlegrid and Multigrid for the 4 cases studied

The results obtained for the 4 cases are similar; that is, ρ_m for Singlegrid converges to the constant 1, while for Multigrid, it consistently remains close to 0 [35, 36].

Accurate solutions can be obtained by combining the Multigrid method with Repeated Richardson Extrapolation (RRE) [47].
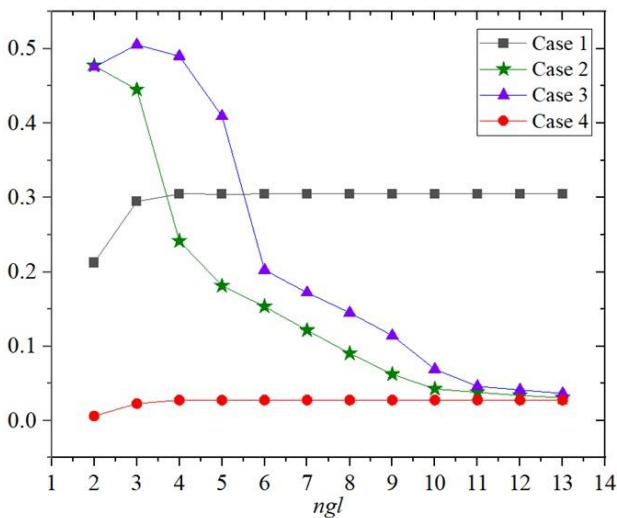
Figure 5. Comparison of ρ_m for Multigrid defined for the 4 cases studied

Figure 5 depicts the average convergence factor (ρ_m) related to 2^{ngl} control volumes for the Multigrid method across the various cases studied.

It is observed that ρ_m for Cases 2, 3, and 4 (realistic values

of K and E) for Multigrid is below 0.1 for the most refined meshes, demonstrating high efficiency. The convergence factor ρ for the first iteration of the Uzawa solver is very efficient, obtaining values tending to 0. However, subsequent iterations do not exhibit the same efficiency, and the average convergence factor ρ_m tends to 0.31 for Case 1, and tends to zero in the other cases studied.

The results of ρ_m in this work are better compared to Luo et al. [26] and Franco et al. [30].

Table 3 presents the number of W-cycles required until the stopping criterion is reached with mesh refinement.

Table 3. Number of W-cycles

Case\ngl	5	6	7	8	9	10	11	12	13
Case 1	16	16	16	16	16	16	16	16	16
Case 2	11	10	9	8	7	6	6	6	6
Case 3	21	12	11	10	9	7	6	6	6
Case 4	6	6	6	6	6	6	6	6	6

From Table 3, it becomes evident that in every case examined, the number of iterations stabilizes with mesh refinement. This is a highly desirable characteristic.

Luo et al. [37] presented the number of cycles W(1,1) ranging from 30 to 45 for different values of hydraulic conductivity, which is three times higher than the number of cycles reported in this paper.

5.2.2 Complexity

Considering the computational time t_{cpu} of the simulations, it is possible to perform a geometric fit to assess the complexity of the algorithm utilizing the equation [14]:

$$t_{cpu} = c \cdot N^\gamma \tag{19}$$

where, c represents a coefficient depending on the method and solver adopted, γ denotes the complexity order of the solver associated with the employed method (graphically, it is the slope of the fitting curve), and $N = N_x \times N_y \times N_t$ is the total number of unknowns of the problem. Theoretically, values of γ close to 1 and c tending to 0 represent better performances of the employed algorithm. Particularly in Multigrid, they mean that CPU time increases linearly with the mesh size. Table 4 presents the results obtained for all cases studied.

Table 4. Parameters γ and c of Eq. (19)

| Case	γ	c
Case 1	1.0303	1.1697×10^{-5}
Case 2	0.9819	9.9678×10^{-6}
Case 3	0.9953	9.3261×10^{-5}
Case 4	1.0031	6.8265×10^{-6}

The complexity presented agrees with the findings in the literature [35, 36].

5.2.3 Computational time and speed-up

In this section, our objective is to assess the performance of both the Singlegrid and Multigrid methods, employing computational time (t_{cpu}) and speed-up (S) as pivotal metrics.

In Figure 6, the computational time t_{cpu}, in seconds, is depicted with mesh refinement using both the Singlegrid and Multigrid methods for Cases 1 and 4. It is evident that the Singlegrid time is notably higher compared to Multigrid one

and escalates further with refinement. This trend renders it impractical to execute simulations for problems using Singlegrid with more than $N_x \times N_y = 2^{10} \times 2^{10}$ control volumes in the mesh.
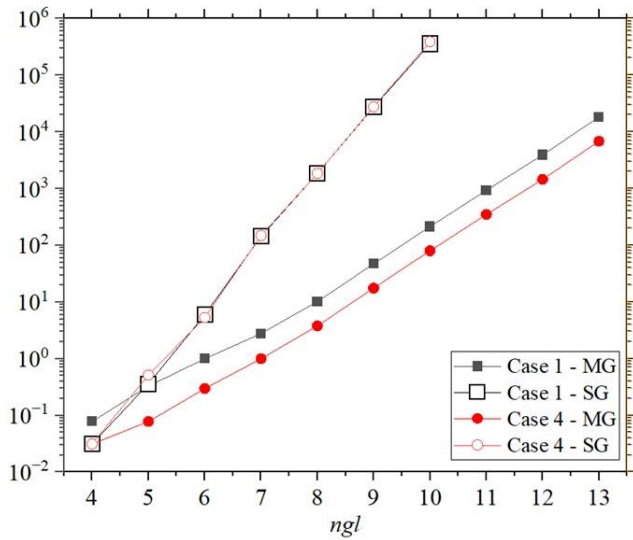
Figure 6. CPU Time for Singlegrid (SG) and Multigrid (MG) with mesh refinement
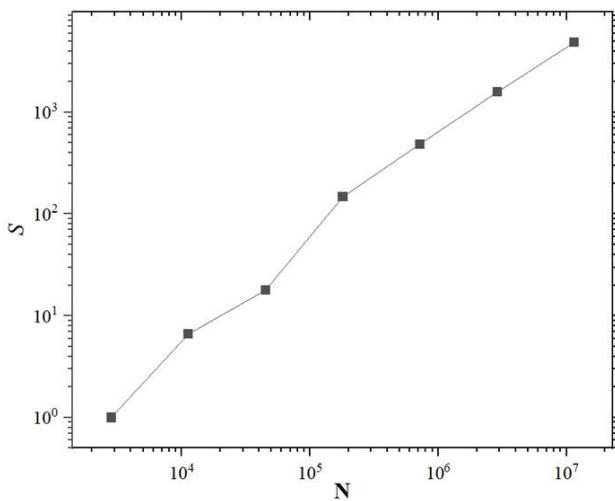
Figure 7. Speed-up for Case 4

Finally, we evaluate the speed-up (S), which is a metric adopted to measure the increase in the speed of the Multigrid algorithm compared to Singlegrid, given by [48]:

$$S = \frac{t_{cpu}(SG)}{t_{cpu}(MG)} \quad (20)$$

Note that from Figure 7, for example, for Case 4 ($K = 10^{-3}$ and $E = 10^6$), with $ngl = 10$ we have $t_{cpu}(SG) = 389514.11$ s, approximately 108 hours, $t_{cpu}(MG) = 79.79$ s, and $S = 4881.74$. This implies a substantial advantage of the Multigrid method, as it is approximately 4881 times faster than the Singlegrid, as evident from Figure 7 for Case 4.

Additionally, the notable increasing behavior of the curve indicates the rise of S with the increase of the number of grid levels ngl, a highly desirable property. Analogous results were achieved for the other cases studied.

The process used in this paper is the same as presented by

Luo et al. [26], applied to the Time Stepping scan, and yielded better results when applied to the new space-time sweep.

In the study conducted by Luo et al. [37], a comparison is made between the Uzawa and Vanka methods, noting that the Uzawa method saves 50% of operations compared to the Vanka method, which justifies the preference for Uzawa. Furthermore, Uzawa is 30% more computationally efficient.

6. CONCLUSION

The mathematical problem of poroelasticity with free drainage was solved by means of discretization using the Finite Volume Method, resulting in a system of partial differential equations for the displacement functions u and v and the pressure function p, which depend on spatial variables, x and y, and the temporal variable, t.

We applied the Uzawa solver in combination with the W-cycle Multigrid method. To address the challenges involving spatial and temporal variables, we introduce a novel space-time sweep.

The key results indicate that:
(1) The average convergence factor tends to values lower than 0.31 when the Multigrid W-cycle method is applied to with realistic constants K and E, validating the effectiveness of the method for these parameters and confirming its robustness.
(2) The computational time with Multigrid is significantly lower compared to Singlegrid, reinforcing the efficiency of the proposed method.
(3) The computational complexity implies that γ approaches 1, while c tends to zero, and the CPU time increases linearly with the number of unknowns [35, 36].
(4) An advantage is the decoupling of the problem-solving process, which would otherwise rely on other solvers, such as Vanka.
(5) The integration of the Uzawa solver with the Multigrid method and the new temporal sweep demonstrates high efficiency and parallelization, with the algorithm fully parallelizable in both space and time.

The impact of this sweep is that it ensures the method performs effectively across a range of realistic values.

These results highlight the computational efficiency of the proposed approach and its capability to effectively address complex poroelasticity problems with accuracy. For example, it facilitates solving problems in geomechanics [8], petroleum engineering [3, 4], biology [11].

Choosing the relaxation parameter ω is crucial, as an improper selection may prevent the method from converging, and it has to be carefully determined [26].

The continuation of this research could further contribute to the development of even more robust algorithms for applications across various engineering disciplines.

REFERENCES

[1] Wang, H. (2000). Theory of Linear Poroelasticity with Applications to Geomechanics and Hydrogeology. Vol. 2, Princeton University Press.

[2] Coussy, O. (2011). Mechanics and Physics of Porous Solids. John Wiley & Sons.

[3] Range, I.L.F., Biot, M.A. (1956). Theory of propagation of elastic waves in a fluid-saturated porous solid. Journal of the Acoustical Society of America, 28(2): 179-191. https://doi.org/10.1121/1.1908241

[4] Haddad, M., Eichhubl, P. (2020). Poroelastic models for fault reactivation in response to concurrent injection and production in stacked reservoirs. Geomechanics for Energy and the Environment, 24: 100181. https://doi.org/10.1016/j.gete.2020.100181

[5] Bear, J. (2013). Dynamics of Fluids in Porous Media. Courier Corporation.

[6] Wu, B., Jiang, L., Liu, Y., Lv, P., Wang, D., Song, Y. (2017). Pore-scale mass transfer experiments in porous media by X-ray CT scanning. Energy Procedia, 105: 5079-5084.
https://doi.org/10.1016/j.egypro.2017.03.1029

[7] Gens, A. (2010). Soil–environment interactions in geotechnical engineering. Géotechnique, 60(1): 3-74. https://doi.org/10.1680/geot.9.P.109

[8] Ammosov, D., Grigorev, A., Stepanov, S., Tyrylgin, A. (2023). Partial learning using partially explicit discretization for multicontinuum/multiscale problems. Fractured poroelastic media simulation. Journal of Computational and Applied Mathematics, 424: 115003. https://doi.org/10.1016/j.cam.2022.115003

[9] Cowin, S. C. (1999). Bone poroelasticity. Journal of Biomechanics, 32(3): 217-238. https://doi.org/10.1016/s0021-9290(98)00161-4

[10] Perrin, E., Bou-Saïd, B., Massi, F. (2019). Numerical modeling of bone as a multiscale poroelastic material by the homogenization technique. Journal of the Mechanical Behavior of Biomedical Materials, 91: 373-382. https://doi.org/10.1016/j.jmbbm.2018.12.015

[11] Tichy, J., Bou-Saïd, B. (2023). A lumped model for long bone behavior based on poroelastic deformation and Darcy flow. Journal of the Mechanical Behavior of Biomedical Materials, 139: 105649. https://doi.org/10.1016/j.jmbbm.2023.105649

[12] He, R., Xiang, Y., Guo, Z. (2023). A poroelastic model for near-field underwater noise caused by offshore monopile driving. Journal of Sound and Vibration, 564: 117878. https://doi.org/10.1016/j.jsv.2023.117878

[13] Rigoni, D., Pinto, M.A., Kwiatkowski Jr, J.E. (2022). Verification and error analysis for the simulation of the grain mass aeration process using the method of manufactured solutions. Biosystems Engineering, 223: 149-160.
https://doi.org/10.1016/j.biosystemseng.2022.08.006

[14] Burden, R., Faires, J. (2016) Numerical Analysis. 10 ed. Cengage Learning.

[15] Versteeg, H.K. (2007). An Introduction to Computational Fluid Dynamics the Finite Volume Method, 2 ed. Pearson Education India.

[16] Yang, A L., Wu, Y.J. (2014). The Uzawa–HSS method for saddle-point problems. Applied Mathematics Letters, 38: 38-42. https://doi.org/10.1016/j.aml.2014.06.018

[17] Oosterlee, C.W., Gaspar, F.J. (2008). Multigrid relaxation methods for systems of saddle point type. Applied Numerical Mathematics, 58(12): 1933-1950. https://doi.org/10.1016/j.apnum.2007.11.014

[18] Borregales, M., Kumar, K., Radu, F.A., Rodrigo, C., Gaspar, F.J. (2019). A partially parallel-in-time fixed-stress splitting method for biot's consolidation model. Computers & Mathematics with Applications, 77(6): 1466-1478.
https://doi.org/10.1016/j.camwa.2018.09.005

[19] Ong, B.W., Schroder, J.B. (2020). Applications of time parallelization. Computing and Visualization in Science, 23: 11. https://doi.org/10.1007/s00791-020-00331-4

[20] Franco, S.R., Pinto, M.A.V. (2024). A space-time multigrid method for poroelasticity equations with random hydraulic conductivity. Numerical Heat Transfer, Part B: Fundamentals, 85(9): 1226-1235. https://doi.org/10.1080/10407790.2023.2262746

[21] Adler, J.H., Gaspar, F.J., Hu, X., Ohm, P., Rodrigo, C., Zikatanov, L.T. (2020). Robust preconditioners for a new stabilized discretization of the poroelastic equations. SIAM Journal on Scientific Computing, 42(3): B761-B791. https://doi.org/10.1137/19M1261250

[22] Miao, S.X., Zhang, J. (2020). On Uzawa-SSI method for non-Hermitian saddle point problems. AIMS Mathematics, 5(6): 7301-7315. https://doi.org/10.3934/math.2020467

[23] Axelsson, O., Karátson, J. (2021). Krylov improvements of the Uzawa method for Stokes type operator matrices. Numerische Mathematik, 148: 611-631. https://doi.org/10.1007/s00211-021-01208-5

[24] Keram, A., Huang, P. (2022). A Uzawa-type iterative algorithm for the stationary natural convection model. Entropy, 24(4): 543. https://doi.org/10.3390/e24040543

[25] Wu, B., Gao, X.B. (2023). A block-diagonally preconditioned Uzawa splitting iteration method for solving a class of saddle-point problems. Advances in Mechanical Engineering, 15(6): 16878132231182370. https://doi.org/10.1177/16878132231182370

[26] Luo, P., Rodrigo, C., Gaspar, F.J., Oosterlee, C.W. (2017). On an Uzawa smoother in multigrid for poroelasticity equations. Numerical Linear Algebra with Applications, 24(1): e2074. https://doi.org/10.1002/nla.2074

[27] Badea, L. (2023). Multilevel Uzawa and arrow–Hurwicz algorithms for general saddle point problems. Journal of Optimization Theory and Applications, 198(2): 678-709. https://doi.org/10.1007/s10957-023-02231-2

[28] Spies, L., Olson, L., MacLachlan, S. (2024). Exploiting mesh structure to improve multigrid performance for saddle-point problems. The International Journal of High Performance Computing Applications. https://doi.org/10.1177/10943420241261989

[29] Gaspar, F.J., Lisbona, F.J., Vabishchevich, P. (2003). A finite difference analysis of Biot's consolidation model. Applied Numerical Mathematics, 44(4): 487-506. https://doi.org/10.1016/S0168-9274(02)00190-3

[30] Franco, S.R., Rodrigo, C., Gaspar, F.J., Pinto, M.A.V. (2018). A multigrid waveform relaxation method for solving the poroelasticity equations. Computational and Applied Mathematics, 37: 4805-4820. https://doi.org/10.1007/s40314-018-0603-9

[31] Luo, P., Rodrigo, C., Gaspar, F.J., Oosterlee, C.W. (2018). Monolithic multigrid method for the coupled Stokes flow and deformable porous medium system.

Journal of Computational Physics, 353: 148-168. https://doi.org/10.1016/j.jcp.2017.09.062

[32] Gaspar, F.J., Lisbona, F.J., Oosterlee, C.W., Vabishchevich, P.N. (2007). An efficient multigrid solver for a reformulated version of the poroelasticity system. Computer Methods in Applied Mechanics and Engineering, 196(8): 1447-1457. https://doi.org/10.1016/j.cma.2006.03.020

[33] Kreyszig, E. (1991). Introductory Functional Analysis with Applications (Vol. 17). John Wiley & Sons.

[34] Ranjan, G., Rao, A.S.R. (2011). Basic and Applied Soil Mechanics. New Age International.

[35] Trottenberg, U., Ooesterlee, C.W., Schuller, A. (2001). A Multigrid. San Diego, Academic Press.

[36] Wesseling, P. (1992) An Introduction to Multigrid Methods. John Wiley and Sons.

[37] Luo, P., Rodrigo, C., Gaspar, F.J., Oosterlee, C.W. (2017). Uzawa smoother in multigrid for the coupled porous medium and Stokes flow system. SIAM journal on Scientific Computing, 39(5): S633-S661. https://doi.org/10.1137/16M1076514

[38] Arrow, K.J., Hurwicz, L., Uzawa, H., Chenery, H.B., Johnson, S., Karlin, S. (1958). Studies in Linear and Non-Linear Programming (Vol. 2). Stanford: Stanford University Press.

[39] Cao, Z.H. (2003). Fast Uzawa algorithm for generalized saddle point problems. Applied Numerical Mathematics, 46(2): 157-171. https://doi.org/10.1016/S0168-9274(03)00023-0

[40] Huang, Z.G., Wang, L.G., Xu, Z., Cui, J.J. (2017). The generalized modified shift-splitting preconditioners for nonsymmetric saddle point problems. Applied Mathematics and Computation, 299: 95-118. https://doi.org/10.1016/j.amc.2016.12.008

[41] Malacarne, M.F., Pinto, M.A.V., Romero Franco, S. (2022). Subdomain method in time with waveform relaxation in space applied to the wave equation combined with the multigrid method. Revista Internacional de Métodos Numéricos para Cálculo y Diseño en Ingeniería, 38(3).

[42] Vandewalle, S. (2013). Parallel Multigrid Waveform Relaxation for Parabolic Problems. Springer-Verlag.

[43] Vandewalle, S., Horton, G. (1995). Fourier mode analysis of the multigrid waveform relaxation and time-parallel multigrid methods. Computing, 54(4): 317-330.

[44] Falgout, R.D., Friedhoff, S., Kolev, T.V., MacLachlan, S.P., Schroder, J.B. (2014). Parallel time integration with multigrid. SIAM Journal on Scientific Computing, 36(6): C635-C661. https://doi.org/10.1137/130944230

[45] Falgout, R.D., Friedhoff, S., Kolev, T.V., MacLachlan, S.P., Schroder, J.B., Vandewalle, S. (2017). Multigrid methods with space–time concurrency. Computing and Visualization in Science, 18: 123-143. https://doi.org/10.1007/s00791-017-0283-9

[46] Wienands, R., Gaspar, F.J., Lisbona, F.J., Oosterlee, C.W. (2004). An efficient multigrid solver based on distributive smoothing for poroelasticity equations. Computing, 73: 99-119. https://doi.org/10.1007/s00607-004-0078-y

[47] da Silva, L.P., Rutyna, B.B., Santos Righi, A.R., Villela Pinto, M.A. (2021). High order of accuracy for Poisson equation obtained by grouping of repeated Richardson extrapolation with fourth order schemes. Computer Modeling in Engineering & Sciences, 128(2): 699-715. https://doi.org/10.32604/cmes.2021.014239

[48] Malacarne, M.F., Pinto, M.A., Franco, S.R. (2022). Performance of the multigrid method with time-stepping to solve 1D and 2D wave equations. International Journal for Computational Methods in Engineering Science and Mechanics, 23(1): 45-56. https://doi.org/10.1080/15502287.2021.1910750

NOMENCLATURE

u, v	Displacement (m)
p	Pressure (Pa)
x, y	Spatial position (m)
t	Time coordinate (s)
$\mathcal{U}, \mathcal{V}$	Density of the force applied to the body (N/m^3)
$\mathcal{P}$	Force of fluid injection or extraction within the porous medium (N/m^3)
E	Young's modulus (N/m^2)
K	Hydraulic conductivity (m/s)
h	Spatial step / Spacing between discretized volumes
ngl	Number of grid levels
t_{cpu}	Computational time (s)
S	Speed-up
N	Total number of unknowns
c	Method coefficient
I_h^H, I_H^h	Restriction and prolongation operator
It_{int}	Number of iterations
cycle	Number of cycles in the Multigrid
it_{uv}	Number of iterations on plane xy

Greek symbols

ω	Relaxation parameter
ν	Poisson's ratio
κ	Hydraulic permeability (m^2)
λ, μ	Lamé constants (N/m^2)
τ	Time interval between time steps
Ω	Spatial domain (m^2)
ρ	Asymptotic convergence factor
ρ_m	Average convergence factor
ν_1	Number of pre-smoothing
ν_2	Number of post-smoothing
γ	Complexity order

Subscripts

W, E	West and east neighboring volumes
P	Central volume
S, N	South and north neighboring volumes